Salt supersaturation as accelerator of influenza A virus inactivation in 1-µl droplets

*Aline Schaub[1], Beiping Luo[2], Shannon C. David[1], Irina Glas[3], Liviana K. Klein[2], Laura Costa[1,4], Céline Terrettaz[1,4], Nir Bluvshtein[2], Ghislain Motos[4], Kalliopi Violaki[4], Marie Pohl[3], Walter Hugentobler[4], Athanasios Nenes[4,5], Silke Stertz[3], Ulrich K. Krieger[2], Thomas Peter[2], and Tamar Kohn[1]**

[1]Laboratory of Environmental Virology, School of Architecture, Civil & Environmental Engineering, École Polytechnique Fédérale de Lausanne, Lausanne, Switzerland

[2]Institute for Atmospheric and Climate Science, ETH Zurich, Zurich, Switzerland

[3]Institute of Medical Virology, University of Zurich, Zurich, Switzerland

[4]Laboratory of Atmospheric Processes and their Impacts, School of Architecture, Civil & Environmental Engineering, École Polytechnique Fédérale de Lausanne, Lausanne, Switzerland

[5]Center for The Study of Air Quality and Climate Change, Institute of Chemical Engineering Sciences, Foundation for Research and Technology Hellas, Patras, Greece

*Correspondence: tamar.kohn@epfl.ch

ABSTRACT

Influenza A virus (IAV) spreads through exhaled aerosol particles and larger droplets. Estimating the stability of IAV is challenging and depends on factors such as the respiratory matrix and drying kinetics. Here, we combine kinetic experiments on millimeter-sized saline droplets with a biophysical aerosol model to quantify the impact of NaCl on IAV stability. We show that IAV inactivation is determined by NaCl concentration, which increases during water evaporation and then decreases again when efflorescence occurs. When drying in air with relative humidity RH = 30%, inactivation follows an inverted sigmoidal curve, with inactivation occurring most rapidly when the NaCl concentration exceeds 20 molal immediately prior to efflorescence. Efflorescence reduces the NaCl molality to saturated conditions, resulting in a significantly reduced inactivation rate. We demonstrate that the inactivation rate k depends exponentially on NaCl molality, and after the solution reaches equilibrium, the inactivation proceeds at a first-order rate. Introducing sucrose, an organic co-solute, attenuates IAV inactivation via two mechanisms, firstly by decreasing the NaCl molality during the drying phase, and secondly by a protective effect against the NaCl-induced inactivation. For both pure saline and sucrose-containing droplets, our biophysical model ResAM accurately simulates the inactivation when NaCl molality is used as the only inactivating factor. This study highlights the role of NaCl molality in IAV inactivation and provides a mechanistic basis for the observed inactivation rates.

KEYWORDS: Influenza A virus – Expiratory droplet – Salinity – Airborne transmission – Respiratory organics

SYNOPSIS: This work quantifies the dependence of influenza A virus stability on salt molality in drying droplets and furthers the understanding of airborne virus transmission.

INTRODUCTION

Respiratory viruses such as influenza A virus (IAV) can be transmitted by expiratory aerosol particles and droplets emitted by an infected individual.[1–5] Small particles (up a few μm) can stay airborne for minutes to hours[6] and travel dozens of meters before encountering a new host,[7] while larger droplets (> 100 μm) can travel only a short distance (1-2 m) and settle within seconds.[7] For both aerosol particles and droplets, IAV can only be transmitted if the viruses remain infectious outside the host. Understanding the environmental parameters that modulate IAV infectivity in expiratory particles and droplets is therefore crucial to tackle seasonal flu epidemics as well as worldwide pandemics.

When aerosol particles and droplets are exhaled from the respiratory tract, they leave an environment with a relative humidity (RH) close to 100% and body temperature and instantaneously enter a cooler, dryer environment. In typical indoor environments in temperate climates, RH can be as low as 30% during winter, whereas it is around 50% in summer.[8] The RH,[9–19] the temperature,[20–22] and the initial size and composition of the expiratory particle[23–25] dictate the droplet drying rate and hence the concentration of solutes in the droplets. If the RH is below the efflorescence relative humidity (ERH) of the salts, the salts will effloresce. Moreover, gas exchange with the environment takes place,[25] and liquid-liquid phase separation may occur.[26] These processes modulate the salinity as well as the pH within the particle. We previously found that the pH in small aerosol particles rapidly decreases to around 4 as a result of gas exchange with the surrounding air.[27] This low pH was suggested to be a primary driver of IAV inactivation in aerosol particles in indoor environments.[27,28] In contrast, larger droplets first undergo alkalization[29] up to pH 10 followed by a much slower acidification on the scale of hours,[25] suggesting that IAV inactivation observed in droplets is likely driven by another factor.

Previous studies have suggested an important contribution of salt to virus inactivation in deposited droplets. Specifically, the stability of IAV,[30] bacteriophage MS2,[18] and SARS-CoV-2[20] was found to be low at intermediate RH (50-65%), just above ERH of NaCl (41-51%),[31] where the salinity in the droplets is expected to be maximal. In search for a mechanistic explanation for this observation, Lin

68 and Marr[18] suggested that the cumulative dose (NaCl concentration multiplied by exposure time) of
69 NaCl over a 1-h drying period is the main determinant of virus inactivation in droplets and aerosol
70 particles for bacteriophages MS2 and Φ6. Similarly, Niazi et al.[32,33] showed that rapid evaporation
71 followed by immediate efflorescence does not inactivate IAV and human rhinovirus-16 in airborne
72 aerosol particles, suggesting that a short exposure to high salinity is insufficient to lead to efficient
73 inactivation. An important role of evaporation dynamics on IAV inactivation in droplets was also
74 proposed by French et al.,[23] who observed faster inactivation during the initial evaporation step, while
75 the particle is still liquid, and a slower decay after efflorescence. Likewise, a near-instantaneous 50%
76 loss in SARS-CoV-2 infectivity was observed when efflorescence occurred, followed by a slower
77 inactivation rate.[34,35]

78 Besides salt efflorescence, IAV stability is also dependent on the presence of organic co-solutes in
79 the matrix, which are typically reported to exert protective effects,[30,36] though the underlying
80 mechanisms are not understood. Nevertheless, some organic compounds, such as the saliva
81 constituents lysozyme and lactoferrin, are viricidal and can enhance viral inactivation.[37,38] Finally,
82 Rockey et al.[39] observed a lower IAV stability in saliva droplets than in respiratory mucus droplets,
83 whereby the difference could not be explained by the salt content nor the drying kinetics, but was
84 instead attributed to the morphology of the dried droplets. Overall, the role of salinity, efflorescence
85 and organic co-solutes in IAV inactivation is thus not fully understood, and it remains difficult to
86 predict inactivation in saline droplets, in particular in the presence of organics.

87 The goal of this study was therefore to provide a mechanistic understanding of the role of salt in IAV
88 inactivation in deposited, drying droplets, to explain observed differences in inactivation rates at
89 different RH and solution conditions. To this end, we aimed to establish a predictive relationship
90 between the NaCl concentration in drying droplets and IAV stability, in the presence and absence of
91 organics.

92 MATERIAL AND METHODS

93 **Virus propagation, purification and enumeration**

94 Influenza A virus (IAV) strain A/WSN/33 (H1N1 subtype) was propagated in Madin-Darby Canine
95 Kidney (MDCK) cells and purified by ultracentrifugation as previously described[27] and detailed in
96 the Supporting Information (SI). Virus infectivity was quantified by plaque assay. Briefly, a 12-well
97 plate containing MDCK monolayers was washed with phosphate-buffered saline (PBS;
98 ThermoFisher, 18912014) and infected with IAV samples. The plates were incubated for 72 h (37°C,
99 5% CO_2) and were then fixed and stained as described in the SI to enumerate and determine the virus
100 titer in plaque forming units (PFU)/ml. A negative control without added virus was always performed
101 on an additional plate. The assay limit of quantification (LoQ) was 10 PFU/ml. The total virus
102 concentration was quantified as genome copies (GC)/ml by Reverse Transcription quantitative
103 Polymerase Chain Reaction (RT-qPCR) as detailed in the SI. All RT-qPCR procedures followed
104 MIQE guidelines[40] (see **Table S1**).

105 **Virus inactivation experiments in droplets**

106 While working with real respiratory matrices is the gold standard, we here aimed to ensure tight
107 control on salinity and organic content in our experiments. We therefore chose to work with a model
108 matrix consisting of NaCl at physiological concentration, and sucrose as an organic substance that
109 can modulate the occurrence of efflorescence. We monitored the inactivation of influenza virus strain
110 A/WSN/33 in 1- and 2-µl drying droplets containing NaCl and sucrose at different ratios. A spherical
111 1-µl droplet has a radius of 620 µm and thus represents the upper end of the particle size distribution
112 produced while coughing or speaking.[41,42] This volume also allows to contain a sufficient number of
113 viruses to monitor several orders of magnitude ($\log_{10}$) of inactivation.

114 Experiments were conducted in solution with an initial composition of either 8 g/l (i.e., molality b =
115 0.14 mol/(kg H_2O) = 0.14 molal) NaCl solution (ThermoFisher Scientific, 207790010) or 5.8 g/l (0.14
116 molal) LiCl solution (Acros Organics, 193370010). This salt concentration corresponds to the NaCl

concentration in simulated lung fluid, that was used previously to assess IAV inactivation in a realistic matrix,[27] falls within the range of salt concentrations measured in sputum (5.9–8.9 g/l),[43] and is also really close to the NaCl concentration in PBS (8.12 g/l). Additionally, experiments were conducted in solutions containing 8 g/l NaCl solution supplemented with either 8 g/l (0.023 molal) or 64 g/l (0.187 molal) of sucrose as a model organic (Fisher BioReagents, BP220-1). These sucrose concentrations were chosen based on droplet efflorescence analysis (**Figure S1**), which showed that the lower sucrose concentration allowed for NaCl efflorescence, whereas no efflorescence was observed (by videography or eye) at the higher one. The solutions were all prepared using milli-Q water. Purified virus stock in PBS was spiked into 100 µl of the matrix in a 1.5-ml plastic tube (Sarstedt, 3080521), to achieve a starting concentration in the experimental solution of either 10^7 PFU/ml ("normal titer") or 10^9 PFU/ml ("high titer"). The added volume of PBS (1%) does not influence the final concentration of NaCl, as the NaCl content of PBS corresponds closely to the initial NaCl concentration. The tube was vortexed and kept in a cold tube rack until use.

Inactivation experiments were performed in an environmental chamber (Electro-Tech Systems, 5532) with controlled relative humidity and temperature. Prior to the experiment, the chamber was set at the targeted RH and room temperature (25°C ± 2) and left to equilibrate. Trace gases potentially present in the chamber air (e.g. acids such as HNO_3), which are absorbed by the droplets, have no influence on the inactivation process, as the large volume of the droplets leads to a high dilution. Once equilibrated, 1- or 2-µl droplets were deposited in the wells of a 96-well plate with a non-binding surface (Greiner Bio-One, 655901), one droplet per well. Droplets were then left to dry at 30% or 65% RH (unless mentioned otherwise), and were periodically collected (see below) over the course of up to 180 min. For each time point in an experiment, three droplets were collected. The three droplets that were deposited last were sampled immediately to act as the time = 0 sample. The deposition time (~10 s per droplet) was recorded and accounted for when sampling the time points. In each experiment, a control was performed in the experimental solution in bulk.

142 To sample a droplet, 300 µl of PBSi (PBS for infection; PBS supplemented with 1% P/S, 0.02 mM
143 Mg^{2+}, 0.01 mM Ca^{2+}, and 0.3% bovine serum albumin (BSA, Sigma-Aldrich A1595), with a final pH
144 of ~7.3) were added to the corresponding well. Each droplet was then resuspended by scratching the
145 bottom of the well with a 200-µl pipette for 5 s, followed by up and down pipetting for 5 times,
146 followed by a second round of scratching and pipetting. Then, each sample was aliquoted in 2x 150
147 µl and frozen at -20°C until further quantification by culturing and RT-qPCR. The recovering and
148 freezing processes do not inactivate the virus further. In each experiment, a control was included by
149 sampling 1 µl of the experimental solution directly from the plastic tube at the beginning and at the
150 end of the experiment. The sample was immediately diluted in 300 µl of PBSi. The tube was kept in
151 the environmental chamber during the whole experiment to ensure similar conditions as for the
152 droplets.

153 To account for physical loss of the virus due to attachment to the wells, recovery of the total
154 (infectious plus inactivated) virus from the plate was measured by RT-qPCR. The measured
155 inactivation was then corrected for virus recovery to determine the actual inactivation.

156 **Virus inactivation experiments in bulk**

157 Inactivation in NaCl bulk solutions were performed in triplicate at room temperature, at three different
158 NaCl concentrations (for subsaturated 0.14 molal and 2.8 molal solutions, and for the saturated 6.1
159 molal solution). A purified virus stock in PBS was spiked in 1 ml of each matrix in a 1.5-ml plastic
160 tube to achieve a starting concentration in the experimental solution of 10^7 PFU/ml. The tubes were
161 vortexed and a 5-µl sample was taken immediately and diluted in 495 µl of PBSi. Samples were taken
162 every 2 h for 10 h, and a final time point was taken after 24 h. All the samples were frozen at -20°C
163 immediately after sampling until quantification.

164 **Determination of inactivation rate coefficient**

165 Inactivation rate coefficients of each experimental condition were determined from least square fits
166 to the log-linear portion of the inactivation curve (that is, for droplets, the inactivation occurring in
167 equilibrated droplets, i.e. ≥ 40 min after deposition), assuming first order kinetics,

168 $$\ln \frac{N}{N_0} = -k \cdot t \qquad \textbf{Equation 1}$$

169 Here, N is the number of infectious viruses in a droplet at time t, N_0 is the initial number of viruses
170 in the droplet and k is the inactivation rate coefficient. All replicate experiments of a given
171 experimental condition were pooled. 99%-inactivation times (t_{99}) were determined based on k:

172 $$t_{99} = -\frac{\ln(0.01)}{k} \qquad \textbf{Equation 2}$$

173 Rate coefficients and associated 95% confidence intervals were determined using GraphPad Prism
174 v.10.0.2.

175 **Determination of evaporating droplet radius**

176 The evaporation of the droplets was filmed by a camera (Sony IMX477R) connected to a Raspberry
177 Pi 4 computer (Model B Rev. 1.4) and a power bank (Varta). The camera was positioned 15 cm above
178 the well plate and took a picture every 16 s. The covered area of each droplet was calculated from the
179 pictures using the software ImageJ (version 1.53t). Briefly, the stack of images was cropped around
180 the droplet of interest and was converted to 8-bit type. Then, an auto-threshold using the "triangle"
181 method was applied across the image stack. A particle analysis was performed on the droplet using
182 default settings, yielding the droplet area of each droplet in pixels. This enables the calculation of
183 relative radii of the (circular) area across all images in the stack. Here, radius (r) refers the base of
184 the cap-shaped droplet after being deposited in one of the non-binding wells as measured by video
185 recording paired with ImageJ analysis and normalized by the initial base radius of the droplet (r_0).
186 Obvious outliers within each time course (abnormally low or high values as determined by visual

inspection) were excluded. In addition, to improve readability of the figures, only 1 out of 2 data points are shown in the evaporation phase, and 1 out of 5 data points are shown in the equilibrium phase (tail). The analysis of the droplet base radius had a small relative standard deviation of 2.4% on average for a single droplet, and of 12% across different droplets (**Figure S2**).

Biophysical modeling

We used the Respiratory Aerosol Model ResAM to predict NaCl and sucrose concentrations in the evaporating droplets and to simulate the inactivation kinetics of IAV. ResAM was developed as a spherical shell diffusion model to determine viral inactivation in spherical aerosol particles and droplets, which we generalized here to take account for the nonspherical droplet-in-well symmetry. ResAM is initialized with the starting composition and size of the droplets, as well as the relative humidity, temperature and ventilation in the experimental chamber, and assuming the viruses to be initially homogeneously distributed in the droplet volume. From this initial state, the model simulates the loss of water molecules by gas phase diffusion, the buildup of internal NaCl concentration gradients in the liquid phase, and derives the inactivation rates as function of NaCl molality, taking into account the internal concentration gradients. ResAM is fully described by Luo et al.[27] and the adaptation to non-spherical droplet geometry is described in detail in the SI, where the uncertainties and model limitations are also discussed.

204 RESULTS

205 **IAV inactivation kinetics in efflorescing NaCl droplets**

206 Inactivation kinetics of IAV in 1- and 2-µl aqueous NaCl droplets exposed to an RH of 30% were
207 measured over the course of 60 min, to compare the kinetics in two different droplet sizes.
208 Simultaneously, the droplet size was monitored as a function of time by videography (**Figure 1**).
209 Initially, the droplets were composed of 8 g/l of NaCl, and 1% (by volume of infectious virus in
210 phosphate buffer saline (PBS), reaching a virus titer of 10^7 PFU/ml. After deposition, the droplets
211 shrank slowly due to water loss until the salt visibly effloresced after approximately 20 min in the 1-
212 µl droplets and after 36 min in the 2-µl droplets (**Figure 1A+C**). After efflorescence, the appearance
213 of the droplets, as seen by eye and videography, did not change until the end of the experiment.

214 The inactivation curve of IAV in both droplet sizes initially followed the evaporation kinetics of the
215 droplets and exhibited an inverted sigmoidal shape (**Figure 1B+D**): during the initial phase of
216 exposure to the controlled RH in the gas phase, the volume loss of the droplets is greatest, as there is
217 a large humidity gradient between the air directly above the liquid surfaces and the prescribed RH in
218 the environmental chamber. However, during the initial 5-15 min, the camera barely detected any
219 change in droplet size (**Figure 1A+C**). This is because the droplet flattens out, its contact angle with
220 the surface decreases and its volume rapidly decreases, while the covered base area remains constant.
221 This cannot be detected from the elevated angle of the camera. Only after the contact angle reached
222 a critical small size, also the covered base area contracts until equilibrium between the liquid and gas
223 phase in the chamber is reached (i.e., until the water activity in the solution a_w = RH).

224 Despite the continuous decrease in volume and the increasing salt concentration, IAV remained
225 infectious during the first 15-25 min. This was followed by a short phase of about 5 min during which
226 IAV infectivity plummeted by more than 2-$\log_{10}$. After efflorescence, the inactivation kinetics slowed
227 significantly and showed a constant inactivation rate for the remainder of the experiment, resulting in
228 less than 2-$\log_{10}$ inactivation in the 40 min after efflorescence. In 2-µl droplets, inactivation kinetics

229 were similar to 1-µl, although the initial slow inactivation phase was prolonged to approximately 30
230 min, due to the smaller relative volume change rate and, hence, the later efflorescence of the larger
231 droplets. Control experiments conducted in bulk solutions showed only minor inactivation during the
232 course of the experiment, suggesting that the observed inactivation can be attributed to the droplet
233 environment.

234 Two mechanisms may explain the rapid decease in virus titer. Either, this may be caused by the
235 formation of salt crystals during efflorescence, as suggested in the context of influenza vaccine
236 microneedles[44] and salt-coated filters on surgical masks.[45] Or, alternatively, inactivation may be
237 driven by IAV exposure to high salinity just before efflorescence. The dissolved NaCl concentration
238 increases as the droplet evaporates and massive supersaturations (> 20 molal, see below) are reached
239 prior to efflorescence, exposing the virus to extreme salinity, before it decreases again to the
240 saturation level (6.1 molal) due to efflorescence. The latter mechanism, first hypothesized by Yang
241 et al.,[30] is proven by our finding that substantial inactivation occurs before efflorescence.

242 Furthermore, **Figure 1B+D** suggests that the data scatter is small before efflorescence, but large
243 afterwards. This observation is also consistent with salinity being the main driver of inactivation: the
244 fastest inactivation occurs under the most saline conditions just before efflorescence, and because
245 efflorescence is a stochastic nucleation process, different droplets effloresce at slightly different
246 times. As a consequence, the viruses in these different droplets are exposed to differently high salt
247 concentrations, resulting in different titers in the moment of efflorescence and beyond.

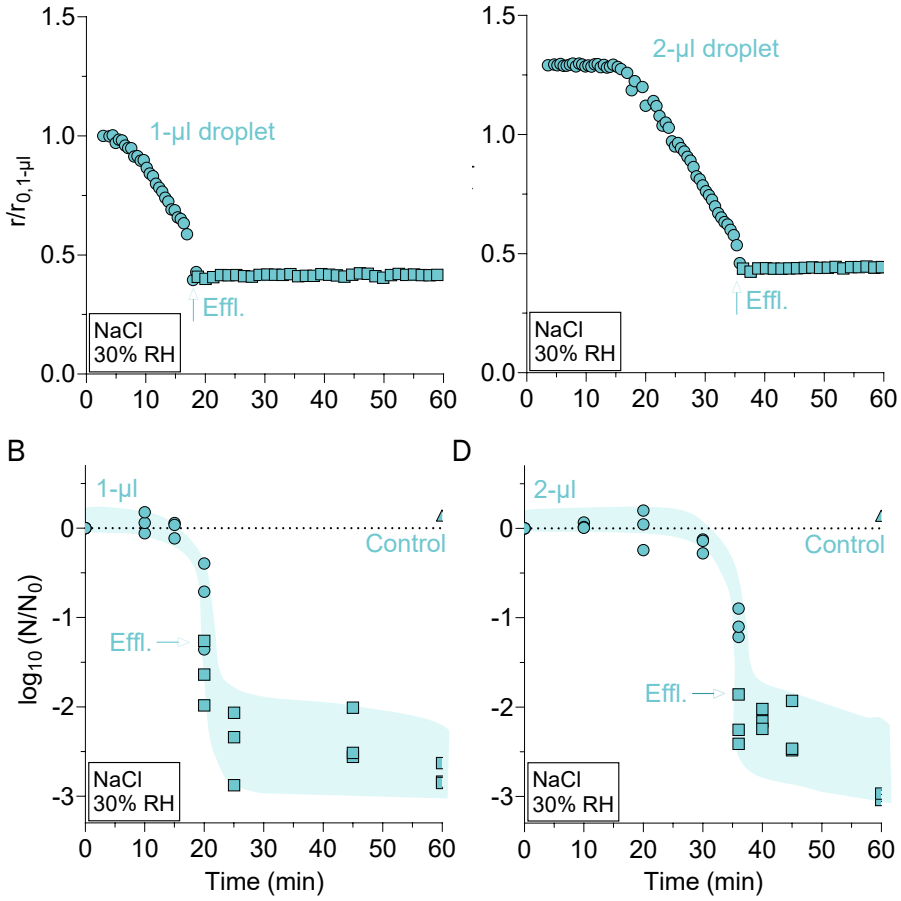

Figure 1: Water loss of highly diluted 1-µl and 2-µl aqueous NaCl droplets ([NaCl]$_{initial}$ = 8 g/l) exposed to 30% RH and concomitant inactivation of IAV in these droplets. Circles represent liquid droplets, squares represent effloresced droplets, and triangles represent control experiments conducted in bulk solution. Efflorescence of NaCl is marked by a green arrow. (A,C) Representative examples of droplet radius shrinkage for one individual droplet with an initial volume of 1 µl (A) and 2 µl (C). Droplet base radius (r) was determined by video recording and was normalized by the initial radius of the 1-µl droplet ($r_{0,1\text{-}\mu l}$). It first decreases due to evaporation and then remains constant after efflorescence. (B,D) Inactivation of IAV in 1-µl (B) and 2-µl (D) droplets. Each data point represents one individual droplet. Shadings serve to guide the eye and to highlight the small data scatter before, and the large scatter after efflorescence caused by small differences in the stochastic nucleation process triggering efflorescence.

IAV inactivation kinetics in non-efflorescing NaCl droplets

To confirm that the main driver of inactivation is high salinity, we tested IAV inactivation under experimental conditions of increasing salt molality but in the absence of efflorescence, combined with droplet size measurements (**Figure 2**). First, experiments were conducted in the same NaCl matrix as in **Figure 1**, but at RH = 65% ≫ ERH (**Figure 2A-B**). Second, inactivation was measured at RH = 30% (same as in **Figure 1**), but in a matrix containing LiCl instead of NaCl (**Figure 2C-D**). LiCl has an ERH of 1-4%,[31] and therefore remains deliquesced at 30% RH. As a reference, experiments in NaCl droplets at 30% RH were also included. In this set of inactivation experiments

267 (but not droplet size measurements), the initial virus titer was increased by 2-$\log_{10}$ compared to the
268 experiments shown in **Figure 1**, in order to increase the detection range. The initial LiCl molal
269 concentration (0.14 m) was identical to the NaCl molal concentration.

270 The inactivation in NaCl droplets at 30% RH followed kinetics comparable to those shown in **Figure**
271 **1**, though efflorescence occurred approximately 5 min earlier than in experiments with a lower virus
272 titer (15 min after deposition instead of 20 min, respectively). This suggests that the presence of
273 concentrated virus can trigger efflorescence (**Figure S3**). The first-order inactivation rate coefficient
274 (k) after efflorescence (time after deposition ≥ 40 min) was 1.8 (± 0.4) × 10^{-2} min^{-1}, corresponding to
275 a time to reach 99% inactivation t_{99} = 260 min (**Table S2**). As explained for **Figure 1C-D**, the large
276 data scatter after efflorescence is to be expected owing to the stochastic nature of the heterogeneous
277 nucleation process.

278 The viral infectivity in NaCl droplets at 65% RH remained stable during 20 min after deposition,
279 consistent with initial conditions of high dilution. Subsequently, it exhibited a first-order inactivation
280 with a rate coefficient k = 6.5 (± 0.4) × 10^{-2} min^{-1}, corresponding to t_{99} ≈ 71 min (**Table S2**). After
281 120 min, IAV inactivation in droplets dried at 30% and 65% RH reached similar levels. In contrast,
282 LiCl droplets at 30% RH exhibited a rapid drop in IAV titer between 10 and 20 min, similar to the
283 time scale in NaCl droplets at the same RH. However, the titer dropped more extensively, and
284 inactivation reached > 5-$\log_{10}$ after 30 min. Thereafter, a reduction in the inactivation rate was
285 observed until 60 min, after which the viral titer was no longer quantifiable. Note that decelerating
286 inactivation curves are often observed in experiments leading to a high titer reduction, and may be
287 explained by the presence of viral aggregates.[46,47] As expected, no efflorescence occurred in the LiCl
288 droplets. Taken together, these experiments indicate that the high salt molality and not the formation
289 of salt crystals causes the inactivation.

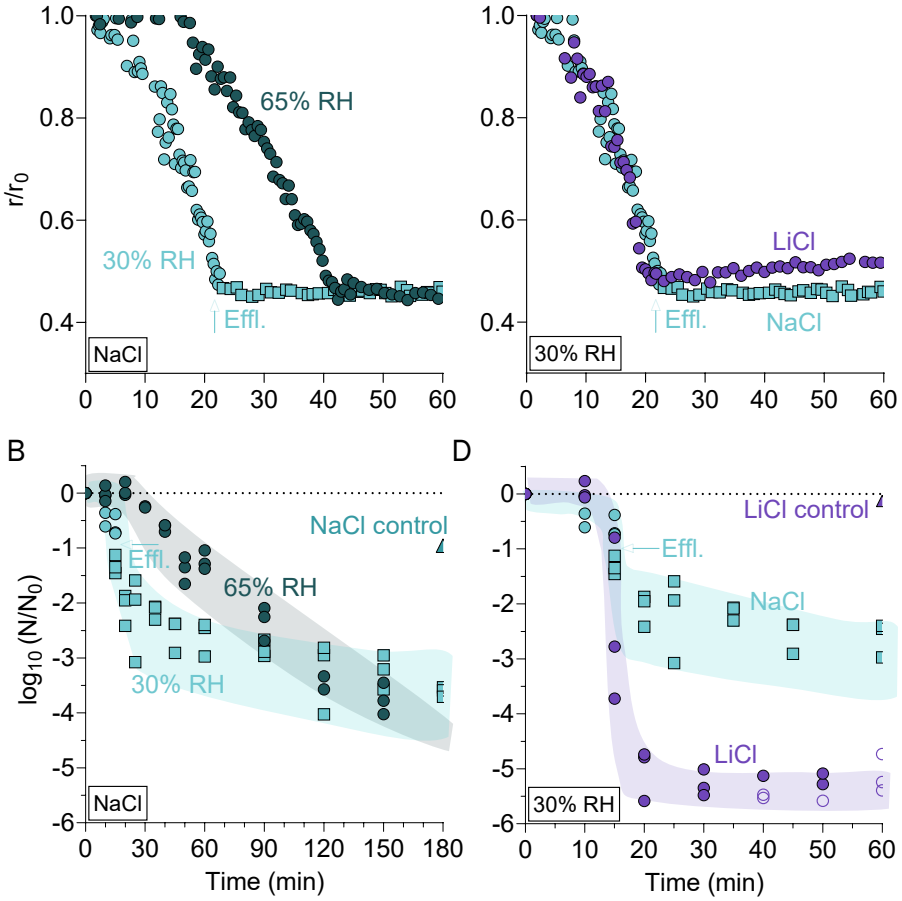

Figure 2: IAV inactivation in 1-µl NaCl droplets at 30% RH (light green) and 65% RH (dark green) for 180 min and in 1-µl LiCl droplets at 30% RH (purple) for 60 min. Circles represent liquid droplets, squares represent effloresced droplets, and triangles represent control experiments conducted in bulk solution. Efflorescence of NaCl (when present) is marked by a green arrow. (A) Representative examples of NaCl droplet radius shrinkage at 30 and 65% RH due to water evaporation until efflorescence (at 30% RH) or liquid-phase equilibrium with air (at 65% RH). Radius (r) was determined by video recording and was normalized by dividing by the initial radius of each droplet (r_0). (B) Inactivation of IAV in 1-µl NaCl droplets ($[NaCl]_{initial}$ = 8 g/l) at 30% RH and 65% RH. Note the longer time scale shown in this panel, as inactivation progressed beyond 60 min. (C) Representative examples of NaCl and LiCl droplet radius shrinkage at 30% RH due to water evaporation until efflorescence (NaCl) or liquid-phase equilibrium with air (LiCl). (D) Inactivation of IAV in 1-µl LiCl droplets ($[LiCl]_{initial}$ = 5.8 g/l) at 30% RH. Empty symbols indicate data below the LoQ. The control for NaCl was taken after 180 min and is shown in panel B. In panels B + D, each data point represents one individual droplet. Shadings serve to guide the eye. Note that the droplet size measurements (panels A and C) were performed at a lower IAV titer and hence efflorescence occurred about 5 min later than in inactivation experiments (see text).

IAV inactivation kinetics in NaCl/sucrose droplets

To assess the inactivation of IAV in the presence of organics, sucrose was added to the NaCl solution. Organics have previously been observed to be protective for IAV in bulk solutions,[27] deposited droplets,[30] or airborne aerosol particles.[36] In these studies, however, the protective matrix was a complex mixture of organics. Here, we chose to use a simple NaCl/sucrose/water system, to be able

311 to determine the concentration of the solutes along the experiment using a biophysical aerosol model
312 (see below). NaCl:sucrose mass ratio of 1:1 and 1:8 were selected (corresponding to 8 and 64 g/l of
313 sucrose, respectively), providing conditions where crystallization occurred (1:1) or was suppressed
314 (1:8) when RH = 30%. The inactivation kinetics of IAV in these two NaCl/sucrose matrices were
315 compared with the inactivation in pure NaCl droplets, here denoted NaCl:sucrose 1:0.

316 After deposition, the 1:1 NaCl:sucrose droplets shrank until efflorescence occurred after 18 min
317 (**Figure 3A**). The inactivation kinetics exhibited an inverted sigmoidal shape, with a fast decay close
318 to the onset of efflorescence, followed by a shallower tail (**Figure 3B**). In the tail, *k* stayed small and
319 constant (slow first-order inactivation) until conclusion of the experiment. The inactivation kinetics
320 was then quite similar to the one observed in 1:0 droplets (though efflorescence in the 1:1 droplets
321 occurred 3 min later and was associated with a larger droplet radius, a smaller drop in titer and slightly
322 slower first-order inactivation rate coefficient in the tail with 1.8 (± 0.4) × 10^{-2} min^{-1} vs. 7.6 (± 3.3) ×
323 10^{-3} min^{-1} for 1:0 and 1:1 ratios, respectively (**Table S2**)). The 1:8 NaCl:sucrose droplets initially
324 shrank at the same rate as the 1:1 droplets but then equilibrated as liquid droplets with the largest
325 relative radius (**Figure 3A**). The inactivation kinetics was slower than in the 1:0 and 1:1 droplets,
326 reaching less than 1-log_{10} inactivation after 180 min, and an inactivation rate coefficient in the tail of
327 6.4 (± 1.7) × 10^{-3} min^{-1} (**Table S2**). In both sucrose-containing droplets, the viruses were thus partially
328 protected from NaCl-mediated inactivation, whereby the protection was greater at a higher sucrose
329 content.

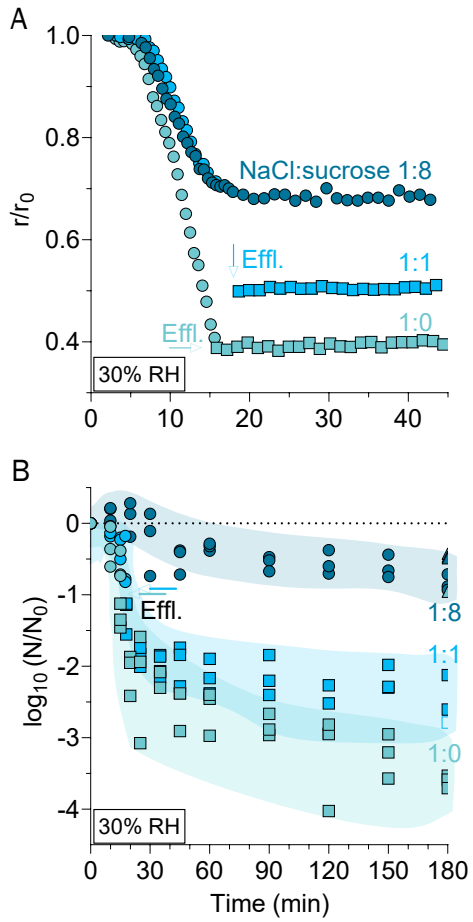

Figure 3: IAV inactivation in 1-µl droplets at 30% RH in various NaCl:sucrose mass ratios. Circles represent liquid droplets, squares represent effloresced droplets, and triangles represent control experiments conducted in bulk solution. Efflorescence, when observed, is indicated by arrows. (A) Representative examples of droplet shrinkage due to water evaporation until efflorescence or liquid-phase equilibrium with chamber RH occurs. Base radius (r) was determined by video recording and was normalized to the initial radius of each droplet (r_0). (B) Inactivation of IAV in 1-µl droplets at three different NaCl:sucrose ratios: 1:0 (light green; $[NaCl]_{initial}$ = 8 g/l, [sucrose] = 0 g/l), 1:1 (light blue; $[NaCl]_{initial}$ = 8 g/l, $[sucrose]_{initial}$ = 8 g/l) and 1:8 (dark blue; $[NaCl]_{initial}$ = 8 g/l, $[sucrose]_{initial}$ = 64 g/l). Each data point represents one individual droplet. Empty symbols indicate data below the LoQ. Shadings serve to guide the eye. Note the different time scales in the two panels for improved readability.

Biophysical model of virus inactivation in drying NaCl/sucrose droplets

The biophysical model ResAM (Respiratory Aerosol Model) was used to simulate the water activity and composition within the droplet as a function of time. A full description of ResAM is available in Luo et al.,[27] and the modifications applied in this study are given in the Supporting Information. In brief, the model is based on a spherical shell diffusion system. However, the droplets in the present work are large (millimeter-sized) and not completely spherical, but to some degree spread out in the wells. Hence, consideration of their flattened shape is required. This is done by describing the flattened droplet with average thickness h as a hemispherical shell with equal thickness concentrically

covering an inert core (see **Figure S4**). To inform the model, IAV inactivation was first parameterized in terms of the NaCl molality and sucrose content. Generally, while the conditions in the droplets change as a function of time, one cannot expect first order inactivation kinetics. Conversely, we assumed that droplets exhibiting first-order inactivation are in equilibrium with the surrounding air. This can occur, for instance, after efflorescence or when the viscosity of the droplets becomes high and the diffusivity within them is low, such that their salt molality no longer changes.

The dependence of inactivation on NaCl molality was determined based on data obtained in both droplet and bulk experiments. Specifically, the molality of any residual fluid in effloresced NaCl droplets following exposure to 30% RH corresponds to saturation molality, i.e. 6.1 mol NaCl/kg H_2O = 6.1 molal,[48] whereas the molality in deliquesced droplets at 65% RH corresponds to a supersaturated state of ca. 8 mol/kg. In agreement with this molality difference, the IAV inactivation rate coefficient k in the residual fluid at 30% RH (after efflorescence) was lower than that measured at 65% (**Figure 2** and **Table S2**). To establish a relationship between NaCl molality and k over a wide molality range, we furthermore measured inactivation in bulk solutions of 0.14, 2.8 and 6.1-mol/kg NaCl (**Figure S5)**. The resulting time courses were well fit by a first-order model, despite a short initial period with faster decay. Finally, the rate coefficient for saturated salt solutions (**Table S2**) was confirmed in a droplet experiment conducted in NaCl at 74% RH (**Figure S6**), where the NaCl molality in the equilibrated droplet corresponds to 6.1 mol/kg. Based on these data, the following exponential relationship between NaCl molality and inactivation rate k (in s^{-1}) and corresponding e-folding time τ could be established (**Figure 4B**):

$$\frac{1}{\tau(m)} = k(m) = k_0 \cdot e^{b/b_0} \qquad \textbf{Equation 3}$$

where b is the molality of NaCl (in mol/(kg H_2O)), b_0 is a fitting parameter corresponding to 2.095 mol/(kg H_2O); and k_0 is the fitted inactivation rate coefficient in pure water, corresponding to $2.5 \cdot 10^{-5}$ s^{-1}.

For sucrose-containing droplets, a similar exponential dependence of k on NaCl molality was assumed, though the absolute value of k at saturation molality was lower due to the protective effect of sucrose exerted in equilibrated droplets (**Figure 3B**). To account for the effect of sucrose, the relationship shown in **Equation 3** was expanded as follows:

$$\frac{1}{\tau(m,x)} = k(m,x) = k_0\{1 + (e^{m/m_0} - 1) \cdot e^{-s_0\, x^{s_1}}\} \qquad \textbf{Equation 4}$$

where x is the mole fraction of sucrose defined as $x = m_{\text{sucrose}}/(m + m_{\text{sucrose}})$, and s_0 = 1.8696 and s_1 = 0.19451 are fitting parameters. For $x = 0$, i.e. in the absence of sucrose, **Equation 4** reduces to **Equation 3**. The inactivation rate in pure water is k_0, while the impact of salt is given by the term $(e^{m/m_0} - 1)$ and protection effect by sucrose by the term $e^{-s_0\, x^{s_1}}$. The fitting parameters in **Equations 3** and **4**, k_0, b_0, s_0 and s_1, were determined by optimizing the output of ResAM to match the measured titers in the NaCl-sucrose solutions, see **Figure 4G-J**. This fitting procedure must also properly account for the diffusivities of H_2O molecules in these solutions (see **Figure 4A**). While appearing arbitrary at first glance, these fitting parameters are actually quite well constrained for water activities $a_w > 0.74$.[49] Mapping the kink in the curves just before efflorescence (**Figure 4G-J**) is a challenge that effectively limits the fitting options (calculations not shown).

Next, ResAM was used to model the water activity and the NaCl molality in the different NaCl droplets. Hereby some assumptions were made: because the inactivation rate coefficient observed in the tail of the pure salt droplet at 30% RH corresponds to that of saturated NaCl solutions (as measured in bulk and in droplets at 74%; see **Figure 4B** and Supporting Information), we conclude that NaCl crystals grow around the virus, forming pockets that limit water evaporation and in which the aqueous salt is saturated. Furthermore, while the 1:8 NaCl:sucrose matrix does not show efflorescence visible by eye, the observed reduction in the inactivation rate after 45 min is indicative of efflorescence. We therefore assume that microscopic dendritic crystal growth occurred in this matrix. This assumption is needed to ensure that the model is consistent with the experimental data. Finally, the model assumes a homogeneous distribution of the virus in the droplet. This is in contrast with studies suggesting that

398 the virus may preferentially localize on the border of the dried droplet when proteins are present in
399 the matrix.[24,39] The exact location of IAV viruses in a drying NaCl/sucrose droplet remains to be
400 assessed.

401 Under these assumptions, ResAM revealed the following: (i) at 65% RH, (**Figure 4C**) the NaCl
402 molality increases up to 8 mol/kg, until equilibrium with air. No efflorescence occurs at this RH, such
403 that the droplet remains supersaturated in NaCl; (ii) at 30% RH (**Figure 4D**), NaCl molality first
404 increases due to water evaporation, and reaches supersaturation (up to 20 mol/kg at the particle
405 surface) before the salt effloresces. After efflorescence, the concentration drops down to saturation
406 molality (i.e., 6.1 mol/kg) and inactivation continues with the same rate as in a saturated bulk solution,
407 likely in pockets of solution encapsulated by crystalline salt; and (iii) in sucrose-containing droplets
408 at 30% RH, the NaCl molality prior to efflorescence is dependent on the sucrose content: the more
409 sucrose, the lower the diffusivity of water and hence the greater the retention of water inside the
410 droplet. (**Figure 4D-F**). After efflorescence, any remaining liquid is in equilibrium with crystalline
411 salt, and hence the aqueous NaCl molality in all matrices corresponds to saturation, i.e. 6.1 mol/kg.
412 The water activities within the drying droplets are shown in **Figure S7.** The diffusion coefficient of
413 water in the different NaCl:sucrose matrices are shown in **Figure 4A**.

414 Finally, by combining the simulated NaCl molality and the molality- and sucrose-dependent
415 inactivation rate coefficient, IAV inactivation was calculated in each shell and at each time point, and
416 the residual virus concentration was integrated over the entire droplet. The resulting inactivation
417 curves correspond well to the measured data in all droplets investigated (**Figure 4G-J**). The model
418 was able to capture the inverted sigmoidal curve of the inactivation in effloresced droplets, the first-
419 order inactivation in deliquesced droplets, and was able to reproduce the protective effect of sucrose.

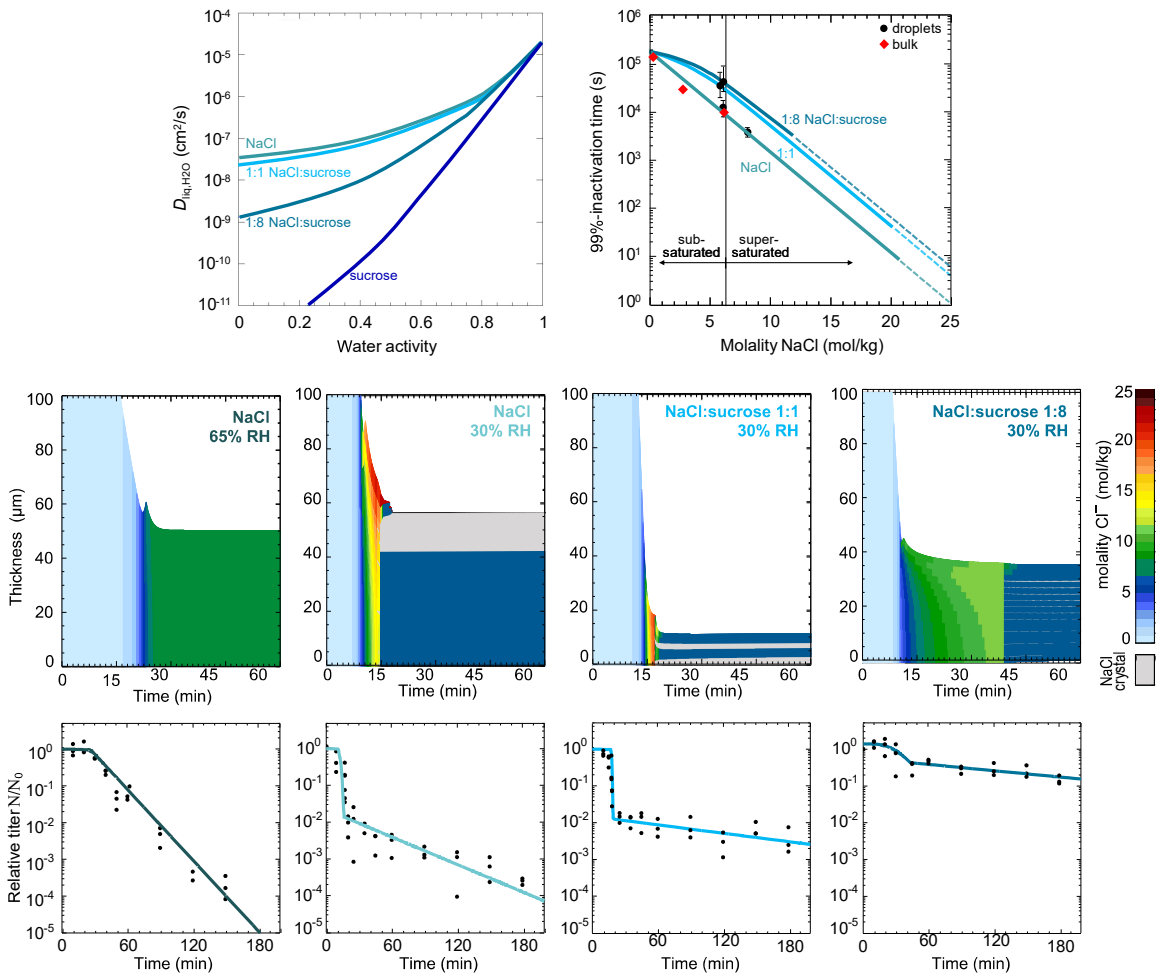

Figure 4: IAV inactivation in deposited droplets modeled with ResAM. (A) Liquid phase diffusion coefficients of H_2O molecules in aqueous NaCl and sucrose solutions and 1:1 and 1:8 dry mass ratio mixtures thereof (see **Equations S1 to S3**). (B) Time required for 99% titer reduction of IAV versus NaCl molality in aqueous NaCl/sucrose droplets derived by fitting ResAM to the experimental data in panels (G-J) and in bulk NaCl solutions. The inactivation times in droplets are based on the first order inactivation rates after droplet compositions stopped changing by equilibration with air, that is ≥ 40 min after deposition. The green line represents the model prediction of 99%-inactivation time according to **Equation 3** for NaCl only. The light blue and dark blue lines are for aqueous NaCl:sucrose mixtures with a dry mass ratio of 1:1 and 1:8, respectively, according to **Equation 4**. (C-F) Evolution of NaCl molality in 1-µl drying droplets with different compositions, modeled with ResAM. At 30% RH, all the droplets reach a final molality of 6.1 mol/kg, corresponding to saturation conditions after efflorescence independent on sucrose content. Light gray regions show the effloresced NaCl crystals, which are modeled as dendrites with average distances of 5 um, as observed by Luo et al.[27] in synthetic lung fluid. In (D) a crust of pure salt hinders the further diffusion of H_2O, whereas in (E,F) the (assumed) salt layers interspersed with sucrose reduce the aqueous NaCl concentration but remain penetrable for H_2O molecules. (G-J) Measured IAV inactivation in 1-µl droplets (black dots) in NaCl at 65% RH (G), NaCl at 30% RH (H), NaCl:sucrose 1:1 at 30% RH (I) and NaCl:sucrose 1:8 at 30% RH (J) and simulated inactivation curve (solid lines) determined using ResAM.

439 **Effect of NaCl on infection cycle and virion integrity**

440 To gain insight into the mechanism of NaCl-induced inactivation, we first conducted fluorescence
441 imaging of viral replication within cells (see Supporting Methods). This is done by fluorescently
442 labeling the influenza nucleoprotein (NP), which is expressed within the host cell's nucleus during
443 the early stages of IAV infection cycle, and is then transported in the cytoplasm at a later stage.[50]
444 Therefore, the presence of NP fluorescence within the nucleus or the cytoplasm of the cells indicates
445 active viral replication, while no signal indicates the virus's incapacity to synthesize NP – i.e., the
446 virus is inactivated. For this purpose, we used sample aliquots from the inactivation experiment in 1-
447 µl NaCl droplets exposed to 30% or 65% RH (**Figure 2B**). At both RH levels, the IAV titer was
448 reduced by ~3-$\log_{10}$ after 120 min. Samples taken at times 0 and 120 min were used to infect A549
449 cells for 6 h, prior to fluorescent staining of the IAV nucleoprotein (NP). A549 cell nuclei were
450 stained with DAPI. Fluorescence microscopy showed that in cells infected with viruses in freshly
451 deposited droplets (exposure time 0 min), NP production was present in approximately half of the
452 cells (**Figure 5A**), indicating that viral replication occurred. However, viruses exposed to 30% or
453 65% RH for 120 min did not show any NP signal 6 h post infection, indicating that the infection cycle
454 was interrupted at an early stage (that is, before the onset of NP protein synthesis).

455 Next, we investigated the integrity of the virions after droplet drying (see Supporting Methods). To
456 this end, 1-µl NaCl droplets were again exposed to 30 and 65% RH, resulting in 1.5-2.5 $\log_{10}$
457 inactivation after 120 min (**Figure 5B-C**). Samples taken at times 0 and 120 min were then incubated
458 for 30 min at 37°C in a digestion mixture (see composition in *Methods*) containing RNase, and the
459 residual RNA copy number was subsequently quantified by RT-qPCR. Hereby the assumption is that
460 if the virion integrity is compromised by exposure to NaCl, the RNase can access and degrade the
461 viral RNA, whereas in intact virions, the RNA is protected.[51] As a control, half the volume of each
462 sample was exposed to the digestion mixture without RNase. In the absence of RNAse, only a minor
463 loss of genome copies was observed over the course of 120 min. In contrast, in the presence of
464 RNAse, approximately 2-$\log_{10}$ decrease in genomic copies was observed after 120 min at both

465 humidities (**Figure 5B-C**, third bar). This decay corresponds well to the observed infectivity decay
466 (**Figure 5B-C**, first bar), suggesting that the disruption of virion integrity is the main inactivation
467 mechanism at high NaCl concentrations.

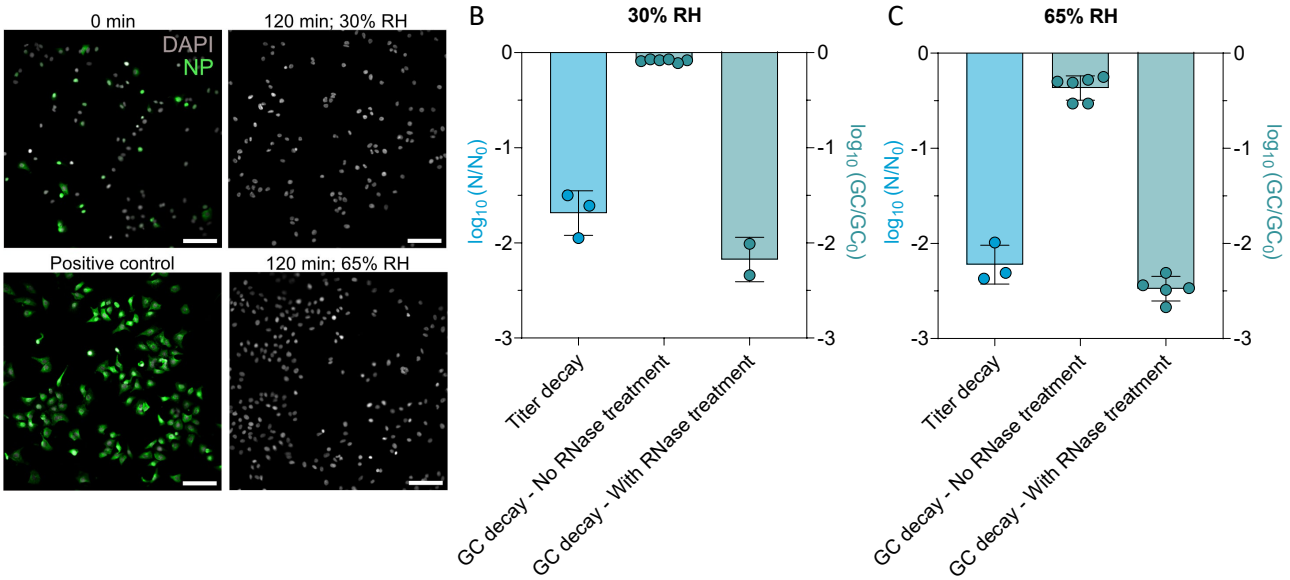

468
469 **Figure 5: Effect of high salinity on IAV infectivity.** (A) Immunofluorescence images of A549 cells infected
470 with IAV samples exposed to 30% or 65% RH in 1-µl NaCl droplets for 120 min. A549 cells were infected at
471 a multiplicity of infection (MOI) of 1, and IAV protein production was visualized by immunofluorescent
472 staining of nucleoprotein at 6 h post-infection. Scale bar corresponds to 100 µm. Images are representative of
473 duplicate experiments. The positive control was infected with a fresh stock of IAV. (B,C) Infectivity decay of
474 IAV samples exposed to 30% (B) or 65% RH (C) in 1-µl NaCl droplets for 120 min, and genome quantification
475 by RT-qPCR of these samples incubated with and without RNase for 30 min prior to RNA extraction. Data
476 are presented as the $\log_{10}$ of the ratio between viral concentration after 120-min exposure in droplet and the
477 initial concentration. In case of infectivity measurements, the virus concentration is represented by the titer (in
478 PFU/ml), and in case of RT-qPCR quantification, the virus concentration is represented by the genomic copies
479 (in GC/ml).

480

481 DISCUSSION

482 Salinity, especially the presence of NaCl but also of other salts such as LiCl and KCl, has been
483 proposed as a promoter for the inactivation of viruses,[52–54] yet a comprehensive understanding of the
484 underlying mechanisms and kinetics has remained elusive. In this study, we combined experimental
485 data on IAV inactivation at different salinities with a biophysical model to parameterize the effect of
486 NaCl on virus stability. Our data suggest that the main inactivation driver of IAV in efflorescing
487 saline droplets is exposure to high (supersaturated) NaCl molality rather than the formation of salt
488 crystals during efflorescence. This suggestion was confirmed by model simulations showing that the
489 NaCl molality, which increases dramatically prior to efflorescence and then is reduced to saturation
490 post-efflorescence, is sufficient to explain the observed inactivation.

491 The ResAM model was able to capture the entire inactivation curve observed in both effloresced and
492 deliquesced droplets, and in both aqueous NaCl and NaCl/sucrose matrices. A recent study proposed
493 the inactivation of bacteriophage MS2 to be correlated with the cumulative dose, defined as the solute
494 concentration multiplied by the exposure time.[18] A dose-dependent inactivation could not be
495 confirmed by ResAM for IAV. Instead, we here demonstrate an exponential dependence of IAV
496 inactivation on salt molality, suggesting that an increase in molality leads to a disproportionate
497 increase in inactivation. In particular at salt molalities > 20 mol/kg, inactivation times become very
498 fast, with 99% inactivation achieved within seconds. However, even at a RH as low as 30%, it takes
499 several minutes to reach such molalities in 1-µl NaCl droplets, and in droplets containing large
500 amounts of organics, such molalities may not be reached at all. Depending on the RH and the organic
501 content, the virus may thus remain stable for minutes to hours. Therefore, droplet transmission may
502 play an important role in the spread of IAV, and a combination of prevention strategies addressing
503 both aerosol (e.g. ventilation) and droplet transmission (e.g. surface disinfection), may be needed to
504 prevent the spread of influenza.

While our results were obtained in millimeter-sized deposited droplets, our findings are also relevant to smaller, airborne particles with diameters up to few micrometers. Below the deliquescence RH (74%), such particles can rapidly reach supersaturated salt concentrations, similar to those obtained in our experimental system (but experimentally inaccessible in bulk solutions). As shown in our experiments with sucrose, supersaturation is also achieved in matrices with high amounts of organics. We therefore expect that the observed dependence of IAV stability on NaCl molality also applies to smaller particles, including organic-rich expiratory aerosol particles. Depending on the composition of the respiratory matrix and the surrounding air, however, the inactivating effect of NaCl in such small particles may be outcompeted by other inactivating factors, including aerosol pH. Specifically, virus inactivation in small particles was previously suggested to be driven by acidic[27] or basic[29] pH, though the contribution of pH-mediated inactivation mechanism remains to be confirmed in real world systems. In contrast, acidification in millimeter-sized droplets is too slow to compete with salt-mediated inactivation,[27] and we found IAV to be stable over the course of 1 h at an alkaline pH of 11 (**Figure S8**). We can therefore exclude pH as a determinant of virus inactivation in droplets, highlighting the importance of salinity in modulating virus stability.

The inactivation of IAV in drying droplets may be explained by a combined effect of two processes: the removal of water molecules due to evaporation, and the subsequent increase of salt molality. Our data suggest that the virion integrity is damaged in drying NaCl droplets (**Figure 5**). Virion integrity loss was also observed to be a minor mechanism in the inactivation of IAV by acidic pH, as encountered in small aerosol particles.[51] For salinity-mediated inactivation in drying droplets, however, damage to the virus structure seems to be the main inactivation mechanism. Therefore, we here summarize how these two processes may affect the lipid envelope and the viral proteins.

Upon drying, the osmotic pressure induced by the solutes increases and causes shrinkage of IAV by forcing water molecules to exit the virus.[55] The shrinkage rate constant of influenza virus was previously observed to increase with ionic strength, until reaching a threshold where the lipids and the matrix proteins (M1) are no longer able to adapt to the compressive stress, resulting in

531 morphological change and loss of membrane integrity.[55] This concurs with our finding that damage
532 to the viral integrity is the main inactivation mechanism. The authors furthermore hypothesize that
533 the morphological change in the membrane leads to irreversible conformational changes, resulting in
534 the loss of hemagglutinin (HA) activity. We did not investigate the structural integrity and
535 functionality of HA in this work, though it is possible that this mechanism occurs concomitantly to
536 the loss of virion integrity in drying saline droplets.

537 In addition to osmotic stress, water evaporation may induce leakage of the viral lipid envelope. It was
538 shown that when the water molecules surrounding the phosphate heads of membrane phospholipids
539 are removed, the packing of the head groups densifies. The subsequent increase of Van der Waals'
540 interactions among hydrocarbon chains trigger a phase transition in the lipid bilayer.[56,57] Specifically,
541 under physiological conditions, the phase transition temperature, (T_m) is usually below room
542 temperature, and the hydrated lipids are in a disordered, flexible liquid crystalline phase. However,
543 the increase of Van der Waals' interactions due to water removal increases T_m to values above room
544 temperature and forces the dried lipids to transition into an ordered, solid-like gel phase. Upon
545 rehydration, the lipids then undergo a reverse phase transition when the head group packing decreases
546 due to the formation of H-bonds with water. These phase transitions induce leakage of the lipid
547 bilayer, damaging the membrane. We hypothesize that a similar mechanism occurs in the viral
548 envelope of influenza virus in a drying droplet or aerosol particle, with rehydration occurring when
549 the particle is inhaled by a host. Moreover, both Na^+ and Cl^- ions were found to bind with the lipid
550 head groups, increasing the ordering of the lipids and subsequently increasing T_m.[58–61] We propose
551 that the combination of water removal and NaCl attachment to the lipid bilayer promote phase
552 transition and cause damage to the viral envelope, which may interfere with fusion during viral
553 infection. Such a mechanism agrees with our data that demonstrate that in drying droplets, IAV
554 inactivation is driven by high NaCl molality and is caused by damaging the virion integrity. It is also
555 consistent with findings by Lin et al.,[62] who observed a higher salt susceptibility of the enveloped
556 bacteriophage Φ6 than the non-enveloped bacteriophage MS2, supporting the hypothesis of viral

557 envelope disruption by high salinity. Similarly, Kukkaro and Bamford[63] saw a larger sensitivity to
558 NaCl concentration changes of enveloped viruses compared to non-enveloped ones. Nevertheless, to
559 conclusively confirm this mechanism, future work should study phase transition mechanism in the
560 lipid bilayers of enveloped viruses in drying droplets.

561 We observed that the addition of sucrose is protective for IAV in drying droplets (**Figure 3B**). The
562 protective mechanism by sucrose is two-fold. First, as shown in **Figure 4**, the presence of sucrose in
563 the matrix decreases the molality of NaCl during the drying phase, thereby lowering viral inactivation.
564 This effect is particularly evident at an NaCl:sucrose ratio of 1:8, and constitutes an indirect protective
565 effect from sucrose. Second, our results show that sucrose also has a direct protective mechanism: in
566 droplets at equilibrium, the NaCl molality is independent of the sucrose concentration (**Figure 4B**),
567 and yet lower inactivation rate coefficients are observed when sucrose is present (**Table S2**). The
568 inactivation rate coefficients follow the trend 1:0 > 1:1 > 1:8 (**Figure 4H-J**), showing that an
569 increasing sucrose concentration increases the protection. Here, the protection cannot be attributed to
570 a change in NaCl molality, as the latter is at saturation in all conditions. Therefore, a different, direct
571 mechanism must protect the virus.

572 Potential direct protection mechanisms by sucrose acting on both lipids and proteins are described in
573 the literature. The addition of disaccharides, such as sucrose and trehalose, was previously shown to
574 help stabilize the membrane phospholipids during lyophilization.[56,57,64] The sugar molecules interact
575 with the phosphates, inserting in between the head groups and replacing water. The packing density
576 needs to decrease to give room to the sugars, and the Van der Waals' interactions are reduced.
577 Consequently, T_m is decreased, and remains below room temperature. Therefore, despite water
578 removal, the lipids do not undergo phase transition, and no membrane leakage occurs. The direct
579 protection of IAV exerted by sucrose in the droplet may thus be partly due to the protection of the
580 lipid bilayer from water loss, preventing the damage to the lipid envelope during drying. In addition,
581 the sucrose may also protect the lipid bilayer from the effects of salt, if sucrose replaces the Na^+ and
582 Cl^- ions between the lipid head groups and thereby counteracts the increase in T_m caused by the salt.

583 This mechanism remains to be assessed, but it correlates with the decrease in inactivation rate as a
584 function of sucrose content in matrices with similar NaCl molalities (**Figure 4H-J**).

585 Additionally, protection may arise from the stabilization of surface proteins by sucrose.[65–68] Upon
586 drying, the water molecules stabilizing the structure of proteins are removed, unfolding the proteins
587 and inducing potentially irreversible conformational changes.[66,69] However, when osmolytes (here,
588 sucrose) are present, they are sterically excluded from the first hydration shell of the proteins. This
589 preferential exclusion of the sucrose leads to a preferential hydration of the proteins, increasing the
590 free energy of the system. The unfolded state of the proteins becomes thermodynamically
591 unfavorable, forcing the proteins to remain in their native state. Our data do not indicate whether
592 protein unfolding occurred in drying droplets, and therefore we cannot assess whether the sucrose
593 protection is in fact caused by protein stabilization. Indeed, the surface proteins of a virus have lower
594 mobility than proteins in solution, and it is possible that this stabilization mechanism is less
595 pronounced in viruses. Further studies on IAV are required to confirm this protection mechanism by
596 sucrose and other organics present in respiratory fluids.

597 This study has some limitations. First, the ResAM model used herein relies on some assumptions that
598 remain to be validated. Specifically, the encapsulation of residual water and viruses by NaCl crystals
599 in efflorescing droplets, as well as the formation of micro-crystals in the 1:8 NaCl:sucrose solution,
600 are hypothetical physical processes that need to be assessed. However, previous studies have shown
601 that the viscosity of an organic phase can kinetically limit the coalescence of the inorganic salt
602 crystal,[70] and non-coalesced salt crystals were observed in porcine respiratory fluid,[71] which supports
603 the hypothesis of micro-crystal formation when the sucrose content is large. Moreover, we accounted
604 for the flattened shape of the droplet despite using a spherical model by limiting the diffusion depth
605 to the thickness of the spread droplet. This also represents a minor uncertainty of ResAM, as detailed
606 in the SI. The likely largest uncertainty in ResAM, however, results from the extrapolations of the
607 inactivation times (**Figure 4B**) and the diffusivities (**Figure 4A**) to highly supersaturated regimes
608 without direct measurements. For both these parameters, we conducted sensitivity analyses (see SI

609 and **Figures S9** and **S10**), which reveal that in particular, improved experimental data for diffusivities
610 in highly concentrated salt solutions would be beneficial for further constraining our model
611 assumptions.

612 Finally, the simple NaCl/sucrose/water matrices that were used in this study are useful to parameterize
613 ResAM, but are far less complex than real respiratory fluids and saliva. In real matrices, other
614 processes may occur during droplet drying, such as the formation of a glassy shell by proteins,
615 limiting evaporation.[32] In addition, the morphology of the dried droplet, the importance of which has
616 been recently presented by Rockey et al.,[39] is dependent on the matrix composition, such as the Na:K
617 ratio[71] and the initial NaCl content[34,35] that can affect crystal formation. It is therefore essential to
618 combine studies of both simple and more complex matrices, to disentangle the effects of all
619 parameters and assess their importance for IAV transmission.

620 In summary, we demonstrate that IAV inactivation in deposited droplets is driven by the high NaCl
621 molality due to water evaporation. Furthermore, we propose a model to simulate IAV inactivation in
622 droplets as a function of RH, NaCl and organic concentration. Finally, we determined that organics
623 (sucrose) protect IAV by two mechanisms: first by decreasing the salt molality in the drying droplet
624 and second, by a direct mechanism that may prevent the leakage of the lipid bilayer and the unfolding
625 of surface proteins. This work contributes to the understanding and quantification of virus inactivation
626 in drying droplets. It expands the fundamental knowledge of airborne virus transmission, which is the
627 basis for the development of appropriate mitigation strategies.

628

629 ASSOCIATED CONTENT

630 **Supporting information**

631 The following file is available free of charge and contains:

632 Method descriptions for virus propagation, purification and quantification, nucleoprotein staining by
633 immunofluorescence and RNase assay to test virion integrity; further description of ResAM
634 adaptation to droplets; discussion of ResAM limitations; droplet pictures; additional IAV inactivation
635 kinetic measurements in bulk and in droplets; check-list for RT-qPCR following MIQE guidelines;
636 values of inactivation rate coefficients and corresponding 99%-inactivation times (PDF)

637 AUTHOR INFORMATION

638 **Corresponding Author**

639 Tamar Kohn –Laboratory of Environmental Virology, School of Architecture, Civil & Environmental
640 Engineering, École Polytechnique Fédérale de Lausanne (EPFL), CH-1015 Lausanne, Switzerland –
641 tamar.kohn@epfl.ch

642 **Author Contributions**

643 Conceptualization: AS, TK, TP, UKK

644 Methodology: AS, BL, IG, LKK, SCD, TK, TP, UKK

645 Software: BL

646 Formal analysis: AS, BL, TP

647 Investigation: AS, BL, IG, LC, SCD

648 Resources: UKK, SSt, TK

649 Writing–original draft: AS, BL, TK, TP

650 Writing–review & editing: AS, BL, CT, GM, IG, KV, LKK, MP, NB, SCD, SSt, TP, TK, UKK

651 Visualization: AS, BL, IG, LKK, TK, TP

652 Supervision: SSt, TK, TP, UKK

Project administration: TK

Funding acquisition: AN, SSt, TK, TP, UKK, WH

Notes

Authors declare that they have no competing interests.

Data availability: Experimental data are available in the public repository Zenodo under the following link: https://zenodo.org/records/10418730. ResAM code will be made available upon manuscript acceptance.

ACKNOWLEDGEMENTS

This work was funded by the Swiss National Science Foundation (grant 189939). The authors thank Sophia Kiselova for assistance with the illustrations.

REFERENCES

1. Tellier, R. Aerosol transmission of influenza A virus: a review of new studies. *J. R. Soc. Interface* **6**, S783–S790 (2009).

2. Cowling, B. J. *et al.* Aerosol transmission is an important mode of influenza A virus spread. *Nat. Commun.* **4**, 1935 (2013).

3. Koster, F. *et al.* Exhaled aerosol transmission of pandemic and seasonal H1N1 influenza viruses in the ferret. *PLoS One* **7**, e33118 (2012).

4. Yan, J. *et al.* Infectious virus in exhaled breath of symptomatic seasonal influenza cases from a college community. *PNAS* **115**, 1081–1086 (2018).

5. Bischoff, W. E., Swett, K., Leng, I. & Peters, T. R. Exposure to influenza virus aerosols during routine patient care. *J. Infect. Dis.* **207**, 1037–1046 (2013).

6. Tellier, R. Review of aerosol transmission of influenza A virus. *Emerg. Infect. Dis.* **12**, 1657–1662 (2006).

7. Dhawan, S. & Biswas, P. Aerosol dynamics model for estimating the risk from short-range airborne transmission and inhalation of expiratory droplets of SARS-CoV-2. *Environ. Sci. Technol.* **55**, 8987–8999 (2021).

8. Verheyen, C. A. & Bourouiba, L. Associations between indoor relative humidity and global COVID-19 outcomes. *J. R. Soc. Interface* **19**, 20210865 (2022).

9. Shechmeister, I. L. Studies on the experimental epidemiology of respiratory infections. III. Certain aspects of the behavior of type A influenza virus as an air-borne cloud. *J. Infect. Dis.* **87**, 128–132 (1950).

10. Hemmes, J. H., Winkler, K. C. & Kool, S. M. Virus survival as a seasonal factor in influenza and poliomyelitis. *Nature* **28**, 221–233 (1962).

11. Marr, L. C., Tang, J. W., Van Mullekom, J. & Lakdawala, S. S. Mechanistic insights into the effect of humidity on airborne influenza virus survival, transmission and incidence. *J. R. Soc. Interface* **16**, 20180298 (2019).

12. Harper, G. J. Airborne micro-organisms: survival tests with four viruses. *J. Hyg. (Lond).* **59**, 479–486 (1961).

13. Schaffer, F. L., Soergel, M. E. & Straube, D. C. Survival of airborne influenza virus: effects of propagating host, relative humidity, and composition of spray fluids. *Arch. Virol.* **51**, 263–273 (1976).

14. Schuit, M. *et al.* The influence of simulated sunlight on the inactivation of influenza virus in aerosols. *J. Infect. Dis.* **221**, 372–378 (2020).

15. Schuit, M. *et al.* Airborne SARS-CoV-2 is rapidly inactivated by simulated sunlight. *J. Infect. Dis.* **222**, 564–571 (2020).

16. Ijaz, M. K., Brunner, A. H., Sattar, S. A., Nair, R. C. & Johnson-Lussenburg, C. M. Survival characteristics of airborne human coronavirus 229E. *J. Gen. Virol.* **66**, 2743–2748 (1985).

17. Dabisch, P. *et al.* The influence of temperature, humidity, and simulated sunlight on the infectivity of SARS-CoV-2 in aerosols. *Aerosol Sci. Technol.* **55**, 142–153 (2021).

18. Lin, K. & Marr, L. C. Humidity-dependent decay of viruses, but not bacteria, in aerosols and droplets follows disinfection kinetics. *Environ. Sci. Technol.* **54**, 1024–1032 (2020).

19. Yang, W. & Marr, L. C. Dynamics of Airborne influenza A viruses indoors and dependence on humidity. *PLoS One* **6**, e21481 (2011).

20. Morris, D. H. *et al.* Mechanistic theory predicts the effects of temperature and humidity on inactivation of SARS-CoV-2 and other enveloped viruses. *eLife* **10**, e65902 (2021).

21. Ahlawat, A. *et al.* Impact of chemical properties of human respiratory droplets and aerosol particles on airborne viruses' viability and indoor transmission. *Viruses* **14**, 1497 (2022).

22. Oswin, H. *et al.* Measuring stability of virus in aerosols under varying environmental conditions. *Aerosol Sci. Technol.* **5**, 1315–1320 (2021).

23. French, A. J. *et al.* Environmental stability of enveloped viruses is impacted by the initial volume and evaporation kinetics of droplets. *mBio* **14**, e03452-22 (2023).

24. Huang, Q., Wang, W. & Vikesland, P. J. Implications of the coffee-ring effect on virus infectivity. *Langmuir* **37**, 11260–11268 (2021).

25. Klein, L. K. *et al.* Expiratory aerosol pH is determined by indoor room trace gases and particle size. *PNAS* **119**, e2212140119 (2022).

26. Ciobanu, V. G., Marcolli, C., Krieger, U. K., Weers, U. & Peter, T. Liquid-liquid phase separation in mixed organic/inorganic aerosol particles. *J. Phys. Chem. A* **113**, 10966–10978 (2009).

27. Luo, B. *et al.* Expiratory aerosol pH: the overlooked driver of airborne virus inactivation. *Environ. Sci. Technol.* **57**, 486–497 (2023).

28. Schaub, A. Expiratory aerosol pH is a driver of the persistence of airborne influenza A virus. *Chimia* **77**, 196–200 (2023).

29. Oswin, H. P. *et al.* The dynamics of SARS-CoV-2 infectivity with changes in aerosol microenvironment. *PNAS* **119**, e2200109119 (2022).

30. Yang, W., Elankumaran, S. & Marr, L. C. Relationship between humidity and influenza A viability in droplets and implications for influenza's seasonality. *PLoS One* **7**, e46789 (2012).

31. Peng, C., Chen, L. & Tang, M. A database for deliquescence and efflorescence relative humidities of compounds with atmospheric relevance. *Fundam. Res.* **2**, 578–587 (2022).

32. Niazi, S. *et al.* Humidity-dependent survival of an airborne influenza A virus: Practical implications for controlling airborne viruses. *Environ. Sci. Technol. Lett.* **8**, 412–418 (2021).

33. Niazi, S. *et al.* Susceptibility of an airborne common cold virus to relative humidity. *Environ. Sci. Technol.* **55**, 499–508 (2021).

34. Haddrell, A. *et al.* Ambient carbon dioxide concentration correlates with SARS-CoV-2 aerostability and infection risk. *Res. Sq.* **preprint**, (2023).

35. Haddrell, A. *et al.* Differences in airborne stability of SARS-CoV-2 variants of concern is impacted by alkalinity of surrogates of respiratory aerosol. *Interface* **20**, 20230062 (2023).

36. Kormuth, K. A. *et al.* Influenza virus infectivity is retained in aerosols and droplets independent of relative humidity. *J. Infect. Dis.* **218**, 739–747 (2018).

37. Kong, Z. *et al.* Virus dynamics and decay in evaporating human saliva droplets on fomites. *Environ. Sci. Technol.* 2c02311 (2022).

38. Malamud, D. *et al.* Antiviral activities in human saliva. *Adv. Dent. Res.* **23**, 34–37 (2011).

39. Rockey, N. C., Le Sage, V., Marr, L. C. & Lakdawala, S. S. Seasonal influenza viruses decay more rapidly at intermediate humidity in droplets containing saliva compared to respiratory mucus. *bioRxiv* **preprint**, 2023–07 (2023).

40. Bustin, S. A. *et al.* The MIQE guidelines: minimum information for publication of quantitative real-

747 time PCR experiments. *Clin. Chem.* **55**, 611–622 (2009).

748 41. Pöhlker, M. L. *et al.* Respiratory aerosols and droplets in the transmission of infectious diseases. *Rev.*
749 *Mod. Phys.* **95**, 045001 (2023).

750 42. Chao, C. Y. H. *et al.* Characterization of expiration air jets and droplet size distributions immediately
751 at the mouth opening. *J. Aerosol Sci.* **40**, 122–133 (2009).

752 43. Lapierre, S. G. *et al.* Cystic fibrosis respiratory tract salt concentration: an exploratory cohort study.
753 *Medicine* **96**, e8423 (2017).

754 44. Choi, H. J. *et al.* Stability of influenza vaccine coated onto microneedles. *Biomaterials* **33**, 3756–3769
755 (2012).

756 45. Quan, F., Rubino, I., Lee, S., Koch, B. & Choi, H.-J. Universal and reusable virus deactivation system
757 for respiratory protection. *Sci. Rep.* **7**, 39956 (2017).

758 46. Mattle, M. J. *et al.* Impact of virus aggregation on inactivation by peracetic acid and implications for
759 other disinfectants. *Environ. Sci. Technol.* **45**, 7710–7717 (2011).

760 47. Sharp, D. G., Floyd, R. & Johnson, J. D. Nature of the surviving plaque-forming unit of reovirus in
761 water containing bromine. *Appl. Microbiol.* **29**, 94–101 (1975).

762 48. Lenzi, F., Tran, T.-T. & Teng, T.-T. The water-activity of supersaturated aqueous solutions of NaCl,
763 KCl, and K_2SO_4 at 25° C. *Can. J. Chem.* **53**, 3133–3140 (1975).

764 49. Kestin, J. & Shankland, I. R. Viscosity of aqueous NaCl solutions in the temperature range 25-200 °C
765 and in the pressure range 0.1-30 MPa. *Int. J. Thermophys.* **5**, 241–263 (1984).

766 50. Kao, R. Y. *et al.* Identification of influenza A nucleoprotein as an antiviral target. *Nat. Biotechnol.* **28**,
767 600–605 (2010).

768 51. David, S. C. *et al.* Inactivation mechanisms of influenza A virus under pH conditions encountered in
769 aerosol particles as revealed by whole-virus HDX-MS. *mSphere* **8**, e00226-23 (2023).

770 52. Brown, J. D., Goekjian, G., Poulson, R., Valeika, S. & Stallknecht, D. E. Avian influenza virus in water:
771 infectivity is dependent on pH, salinity and temperature. *Vet. Microbiol.* **136**, 20–26 (2009).

772 53. Benbough, J. E. Some factors affecting the survival of airborne viruses. *J. Gen. Virol.* **10**, 209–220
773 (1971).

774 54. Salo, R. J. & Cliver, D. O. Effect of acid pH, salts, and temperature on the infectivity and physical
775 integrity of enteroviruses. *Arch. Virol.* **52**, 269–282 (1976).

776 55. Choi, H. J. *et al.* Effect of osmotic pressure on the stability of whole inactivated influenza vaccine for
777 coating on microneedles. *PLoS One* **10**, e0134431 (2015).

778 56. Crowe, J. H., Hoekstra, F. A. & Crowe, L. M. Anhydrobiosis. *Annu. Rev. Physiol.* **54**, 579–599 (1992).

779 57. Rockinger, U., Funk, M. & Winter, G. Current approaches of preservation of cells during (freeze-)
780 drying. *J. Pharm. Sci.* **110**, 2873–2893 (2021).

781 58. Lee, S. J., Song, Y. & Baker, N. A. Molecular dynamics simulations of asymmetric NaCI and KCl
782 solutions separated by phosphatidylcholine bilayers: Potential drops and structural changes induced by
783 strong Na^+-lipid interactions and finite size effects. *Biophys. J.* **94**, 3565–3576 (2008).

784 59. Pabst, G. *et al.* Rigidification of neutral lipid bilayers in the presence of salts. *Biophys. J.* **93**, 2688–
785 2696 (2007).

786 60. Pandit, S. A., Bostick, D. & Berkowitz, M. L. Molecular dynamics simulation of a
787 dipalmitoylphosphatidylcholine bilayer with NaCl. *Biophys. J.* **84**, 3743–3750 (2003).

61. Valley, C. C., Perlmutter, J. D., Braun, A. R. & Sachs, J. N. NaCl interactions with phosphatidylcholine bilayers do not alter membrane structure but induce long-range ordering of ions and water. *J. Membr. Biol.* **244**, 35–42 (2011).

62. Lin, K., Schulte, C. R. & Marr, L. C. Survival of MS2 and Φ6 viruses in droplets as a function of relative humidity, pH, and salt, protein, and surfactant concentrations. *PLoS ONE* **15**, (2020).

63. Kukkaro, P. & Bamford, D. H. Virus-host interactions in environments with a wide range of ionic strengths. *Environ. Microbiol. Rep.* **1**, 71–77 (2009).

64. Chen, C., Han, D., Cai, C. & Tang, X. An overview of liposome lyophilization and its future potential. *J. Control. Release* **142**, 299–311 (2010).

65. Liu, F. F., Ji, L., Zhang, L., Dong, X. Y. & Sun, Y. Molecular basis for polyol-induced protein stability revealed by molecular dynamics simulations. *J. Chem. Phys.* **132**, 225103 (2010).

66. Singh, S. K. Sucrose and trehalose in therapeutic protein formulations. in *Challenges in Protein Product Development* 63–95 (2018).

67. Timasheff, S. N. The control of protein stability and association by weak interactions with water: how do solvents affect these processes. *Annu. Rev. Biophys. Biomol. Struct.* **22**, 67–97 (1993).

68. Lee, J. C. & Timasheff, S. N. The stabilization of proteins by sucrose. *J. Biol. Chem.* **256**, 7193–7201 (1981).

69. Minhaz Ud-Dean, S. M. Structural explanation for the effect of humidity on persistence of airborne virus: Seasonality of influenza. *J. Theor. Biol.* **264**, 822–829 (2010).

70. Fard, M. M., Krieger, U. K. & Peter, T. Kinetic limitation to inorganic ion diffusivity and to coalescence of inorganic inclusions in viscous liquid-liquid phase-separated particles. *J. Phys. Chem. A* **121**, 9284–9296 (2017).

71. Groth, R., Niazi, S., Spann, K., Johnson, G. R. & Ristovski, Z. Physicochemical characterization of porcine respiratory aerosol and considerations for future aerovirology. *PNAS Nexus* **2**, 1–10 (2023).